nature communications

Article

https://doi.org/10.1038/s41467-025-60846-7

MXene Templated assembly of hierarchical Al/CuO/V_2C nanothermite with excellent energy release efficiency and highly tunable performance

Received: 5 September 2024

Accepted: 4 June 2025

Published online: 01 July 2025

Check for updates

Momang Tian[1], Ke-Juan Meng[1], Kunyu Xiong[1], Iftikhar Hussain[1], Xinwen Ma[1] & Kaili Zhang[1,2,3]

Nanothermite has gained significant attention for its exceptional energy release rate and reactivity, making it a promising material for energetic applications. However, nanoparticle agglomeration significantly hinders its energy release efficiency. To overcome this challenge, we developed an innovative bottom-up strategy and a straightforward preparation method to construct a hierarchical Al/CuO/V_2C nanocomposite. This is achieved through the ordered self-assembly of Al and CuO nanoparticles in an ethanol suspension, using V_2C MXene as a template. Our findings show that the Al/CuO/V_2C nanocomposite exhibits distinct morphologies based on V_2C concentration: nanosheets at lower concentrations and microspheres at higher concentrations. CuO and Al nanoparticles form the first and second layers outside the V_2C, respectively, due to the interplay between electrostatic forces and covalent Cu-O-V bonds. This unique structure, along with high reactivity of V_2C, enables complete Al oxidation, achieving a heat release of 3156.2 J g^{-1} with a 10 wt% V_2C addition—seven times greater than the Al/CuO control group. The concentration-dependent structure allows for tunable energetic performance, from a rapid 3-ms deflagration to a prolonged 16-ms combustion. Reduced gas release enhances safety, paving the way for applications in microinitiators and advancing nanothermite technology.

Nanothermite is a new class of energetic materials that has emerged as a result of advancements in nanotechnology. It is widely used in igniters, thrusters, and ammunition[1–3]. Nanothermite combines thermite with nanotechnology, using nanoparticles instead of conventional micro- or larger-sized particles for both oxidizers and aluminum. The primary advantage of this approach is the enhanced energy release rate of the thermite reaction. This improvement arises from the increased surface-to-volume ratio, which enhances reactivity[4–6]. However, the large surface area of nano-sized aluminum and oxidizers introduces additional surface energy. This leads to spontaneous nanoparticle agglomeration as a way to reduce energy, which significantly impairs the energy release efficiency of nanothermite[7,8].

Significant efforts have been made to reduce the agglomeration of nano Al and oxidizer particles, aiming for a more even mixing between Al and oxidizer. These methods can be classified into two types based on whether additives are used. For additive-free

[1]Department of Mechanical Engineering, City University of Hong Kong, Hong Kong, China. [2]Hong Kong Branch of National Precious Metals Material Engineering Research Centre, City University of Hong Kong, Hong Kong, China. [3]City University of Hong Kong Shenzhen Research Institute, Shenzhen, China. e-mail: kaizhang@cityu.edu.hk

approaches, top-down micromachining methods are typically employed during fabrication, such as magnetic sputtering[9,10], E-beam evaporation[11,12], electrospray[13], and electrospinning[14]. These techniques achieve homogeneity through multilayer or core-shell structures and are compatible with integrated circuits (IC) and microelectromechanical systems (MEMS) manufacturing, potentially integrating into chips. However, these methods often introduce alumina passivation layers at Al/oxidizer interfaces in air, which can hinder the reaction process. In addition, they consume significant energy and time[15]. For methods that include additives, a bottom-up strategy is preferred, where the additive acts as a binding agent between Al and oxidizer to build desired nanothermite structures through self-assembly[16], such as core-shell[5] and nanocomposite[17] configurations. These additives effectively reduce nanoparticle agglomeration by preventing adhesion, thereby increasing contact between Al and the oxidizer. Nevertheless, additives often have minimal impact on the thermite reaction while impeding oxygen diffusion. This structural advantage is counteracted by these limitations.

As summarized above, while numerous efforts have been made, both top-down and bottom-up approaches continue to struggle with reducing nanoparticle agglomeration without compromising the energy release efficiency of thermite reactions. To address this challenge, we propose a strategy of fabricating hierarchical nanothermite through the ordered self-assembly of Al and oxidizer nanoparticles, utilizing single-layer MXene as a template. MXenes have garnered significant attention due to their rich surface chemistry, adjustable structures, and abundant surface terminations[18]. MXenes find applications in various fields, including energy storage[19], catalysis[20], electromagnetic shielding[21], and sensing[22]. The negatively charged surface terminations of MXenes offer opportunities for the self-assembly of positively charged Al and oxidizer nanoparticles through long-range electrostatic forces[23]. In addition, the highly reactive surface of MXene enables short-range interfacial covalent bonding with oxidizer particles[24]. During the self-assembly process, when Al, oxidizer, and MXene are present in the suspension, different types of bonding lead to a hierarchical structure. In this structure, oxidizer particles occupy the inner layer, while Al particles take up the outer layer simultaneously. Leveraging the high oxidation tendency of MXene[25,26], such a layered Al/oxidizer/MXene structure can absorb oxygen from the air into MXene and supply it to the oxidizer layer in the thermite reaction. This significantly enhances energy release efficiency.

As a proof-of-concept study, we selected single-layer V_2C MXene as the additive and CuO as the oxidizer. V_2C MXene offers several key advantages: Firstly, V_2C exhibits greater reactivity compared to Ti_3C_2 MXene, providing essential covalent binding sites for CuO to form Cu-O-V interfacial bonds[27,28]. This feature is absent in the commonly used Ti_3C_2 MXene[23]. Secondly, Oxidized V_2C MXene can react with aluminum through an Al/VO_x thermite reaction, generating heat comparable to that of the Al/CuO thermite reaction[29] In contrast, oxidized Ti_3C_2 MXene remains inert and contributes minimally to the total reaction heat. Thirdly, the in-situ formation of VO_x/C structures from high-temperature oxidation of V_2C demonstrates a higher electron transfer rate and catalytic effect than Ti_3C_2. This makes V_2C more effective in catalyzing the Al/CuO reaction at elevated temperatures[30]. Finally, V_2C is currently more accessible than other promising MXenes, such as Mo_2C, in terms of both productivity and cost.

Al/CuO/V_2C was fabricated via a straightforward method involving mixing in an ethanol suspension with sonication. Structural analysis using scanning electron microscopy (SEM) and transmission electron microscopy (TEM) revealed that the structure evolves with varying concentrations of V_2C, resulting in tunable energetic performance. Characterization confirmed successful fabrication through X-ray photoelectron spectroscopy (XPS) and powder X-ray diffraction (PXRD). Thermal properties were verified using differential scanning calorimetry–thermogravimetry (DSC-TG) analysis. Open burn tests demonstrated the catalytic effect of V_2C and its tunable performance across different concentrations. In addition, closed-bomb testing highlighted improved safety and potential applications for micro-initiators. The study also explored the electrostatic and covalent binding mechanisms of Al/CuO/V_2C, alongside discussions on enhancingenergy release efficiency through oxygen diffusion optimization.

Results

Morphological analysis of Al/CuO/V_2C

The Al/CuO/V_2C samples exhibit distinct morphologies depending on the concentration of V_2C MXene suspension used during preparation. At lower concentrations (≤ 5 wt%), the samples form planar structures, while higher concentrations (> 5 wt%) result in spherical morphologies. This variation is attributed to the self-assembly process of CuO and Al nanoparticles with V_2C nanosheets in the suspension. SEM images reveal that at a low concentration (1 wt%), the original shape of the V_2C nanosheet is preserved, with Al and CuO nanoparticles uniformly covering its surface. TEM observations after ultrasonic treatment show a dense attachment of plate-like CuO particles onto the V_2C surface, forming a precursor film. EDS analysis on high-angle annular dark-field scanning transmission electron microscopy (HAADF-STEM) images (Fig. 1d–g and Supplementary Fig. 1) confirms the even distribution of O, V, Al, and Cu across the composite. The similar distribution patterns of Cu and O confirm the presence of CuO. Although Al is detected, its low weight fraction (< 1 wt%) suggests it may be residual from incomplete etching of the MAX phase during V_2C synthesis. High-resolution TEM images (Supplementary Fig. 2) demonstrate the adhesion of CuO on the V_2C surface. The interplanar spacing measurements reveal 0.24 nm for (1 −1 1) plane of CuO and 0.25 nm for (0 −1 1 0) plane of V_2AlC residual, with a contact line marked by a red dashed line[31].

The general morphology of the Al/CuO/V_2C composite changes drastically as the concentration of V_2C increases. In Fig. 1h, microspheres comprised of nano-sized particles are observed. The TEM images (Fig. 1i–m) further unveil the internal structure. It appears that the V_2C nanosheet curls its surface, while the CuO and Al nanoparticles are present both in and out of the envelope. The CuO/V_2C precursor (Fig. 1c) represents a higher binding tendency of CuO nanoparticles to the V_2C surface as both Al and CuO nanoparticles are present in the suspension during the fabrication process. From Fig. 1i, the Al/CuO/V_2C hierarchical structure is clearer as CuO nanoparticles attach to the V_2C surface closely to form CuO/V_2C, while Al particles are surrounded. This indicates an ordered sequence of the assembly of Al/CuO/V_2C rather than a random combination. When both CuO and Al particles are present in the suspension, CuO exhibits a higher tendency to bind on the V_2C surface. The spontaneous self-assembly procedures begin with the formation of CuO/V_2C precursor, and then the resulting Al/CuO/V_2C nanocomposite in both low and high concentration cases. The mapping results prove the existence of both Al (Fig. 1l) and CuO (Fig. 1j, m and Supplementary Fig. 3) particles, indicating the successful incorporation. Recent progress on MXene-based nanocomposites synthesized by electrostatic[32,33] or covalent[34,35] self-assembly methods have shown distinct morphological features. From the TEM and EDS mapping results, the binding characteristics can be distinguished in terms of the overlapping area and distributing uniformity. The electrostatic self-assembled materials tend to show more random alignment and distribution on MXene with less overlapping area because of no selectivity. Therefore, our experiment results suggest the difference of the binding characteristics between Al and CuO towards V_2C, where CuO (Fig. 1j, m) shows a more overlapping area with V_2C (Fig. 1k) and higher distributing uniformity than Al (Fig. 1l).

https://doi.org/10.1038/s41467-025-60846-7

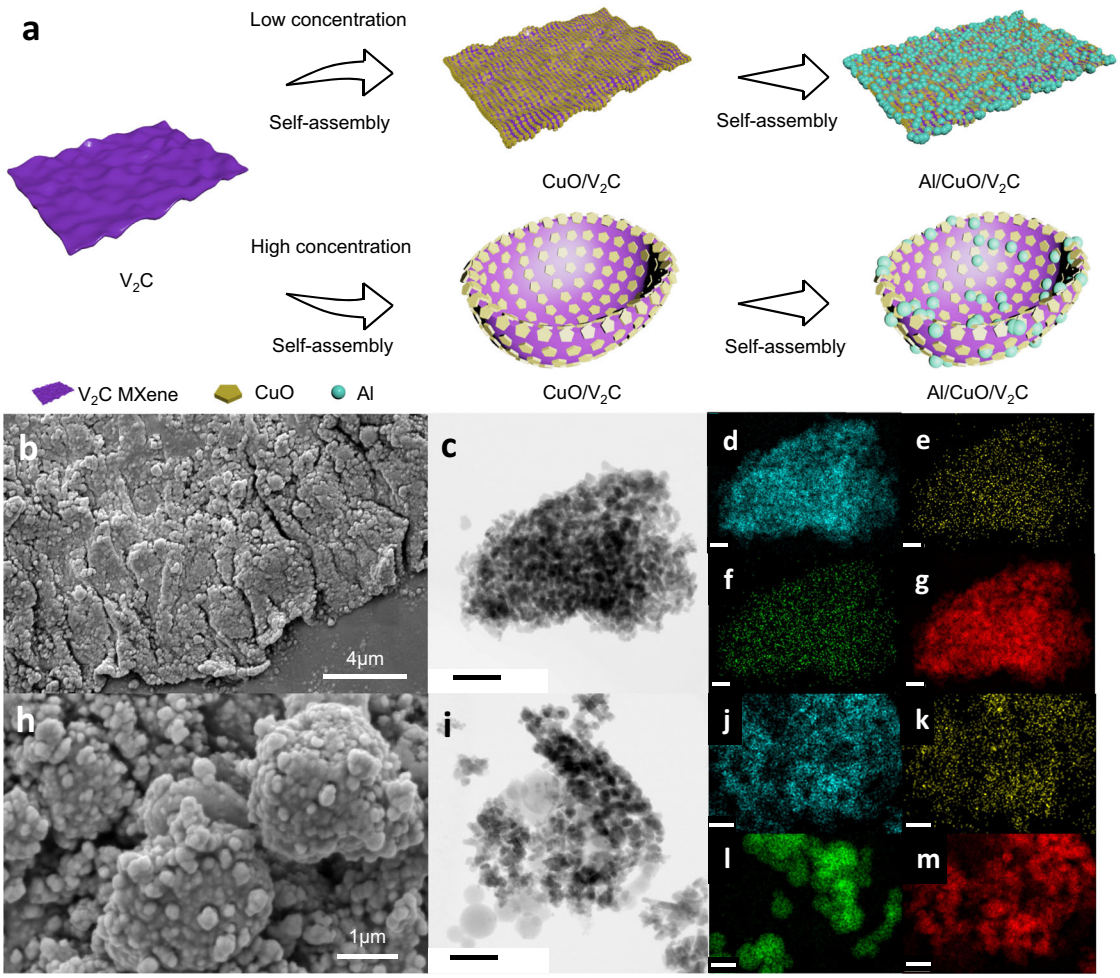

Fig. 1 | Synthesis and morphological analysis of Al/CuO/V_2C. a Schematic illustration for the ordered self-assembly process of the Al/CuO/V_2C in lower and higher concentration cases. **b** The SEM picture of the Al/CuO/V_2C sample with 1 wt% V_2C content. **c**–**g** The TEM picture of CuO/V_2C precursor in the Al/CuO/V_2C sample with 1 wt% V_2C content (**c**) and elemental mapping corresponding to O (**d**), V (**e**), Al (**f**), Cu (**g**) of Al/CuO/V_2C respectively. **h** The SEM picture of the Al/CuO/V_2C sample with 10 wt% V_2C content. **i**–**m** The TEM picture of Al/CuO/V_2C sample with 10 wt% V_2C content (**i**) and elemental mapping corresponding to O (**j**), V (**k**), Al (**l**), Cu (**m**) of Al/CuO/V_2C. Scale bar: for (**c**, **i**), 200 nm; for **d**–**g**, **j**–**m**, 100 nm. The experiments for (**b**–**m**) were repeated three times independently with similar results.

Compositional and Elemental Analysis of Al/CuO/V_2C

To verify the composition of the obtained samples, PXRD and XPS analyses were conducted. The PXRD results (Fig. 2a) confirm that the prepared Al/CuO/V_2C composite contains Al, CuO, and V_2C, as evidenced by characteristic diffraction peaks for each component. The V_2C pattern includes peaks corresponding to both V_2C[36] and V_2AlC[37], with specific Miller indices provided (JCPDS: 29-0101, Supplementary Fig. 4). It is noteworthy that the relative intensity of the V_2C peaks shows a strong dependency on the preparation method of the MXene. The relative intensity of V_2C peaks is influenced by the MXene preparation method; freeze-drying preserves the single-layer structure better, resulting in a higher intensity (0 0 2) peak. The presence of V_2AlC peaks indicates insufficient etching, while their reduction suggests more complete etching[38]. These XRD results align with previously reported findings[39], underscoring the consistency of the observed patterns. The V_2C diffraction peaks are hardly detectable in the Al/CuO/V_2C sample, which is mainly due to low peak intensity, small quantity, and possible overlap with Al and CuO peaks. The XPS survey scan (Fig. 2b) identifies major elements including Al, Cu, O, V, C, and a trace amount of F. The deconvoluted V *2p*/O *1 s* region (Fig. 2c) reveals peaks for C = O, C-O, and Metal-O bonds[40], with the presence of V^{5+} indicating surface oxidation of V_2C after assembly. In the Cu *2p* region (Fig. 2d), Cu^{2+} is observed along with two satellite peaks, confirming that CuO remains in its oxidized state throughout the preparation process.

To gain a deeper understanding of the nanostructure of Al/CuO/V_2C, we etched the composite material (10 wt% V_2C) using argon ions to a depth of 200 nm. The collected data was compared with that obtained before etching[41]. As shown in Fig. 3, only lower oxidation states, such as V^{2+} and V^{3+}, were detected in the V *2p* region after etching. In contrast, prior to etching, only the fully oxidized V^{5+} state was observed. These findings suggest that V_2C is not completely oxidized during the assembly process. A portion of the V_2C structure likely remains as an inner layer without oxidation, while its surface becomes highly oxidized into V^{5+}, forming an outer layer. This oxidation is primarily due to direct contact with CuO and other oxidizing agents. This demonstrates that V_2C retains its activity as an inner layer post-assembly, confirming its role as an active component within the composite structure.

Thermal Analysis of Al/CuO/V_2C

The thermal properties of energetic materials are crucial to their performance and safety characteristics. To investigate these properties, we conducted a DSC-TG analysis on Al/CuO nanocomposites in an air atmosphere, which exhibited exothermic behavior between 500 °C and 850 °C with two distinct peaks (Fig. 4a). The addition of V_2C

https://doi.org/10.1038/s41467-025-60846-7

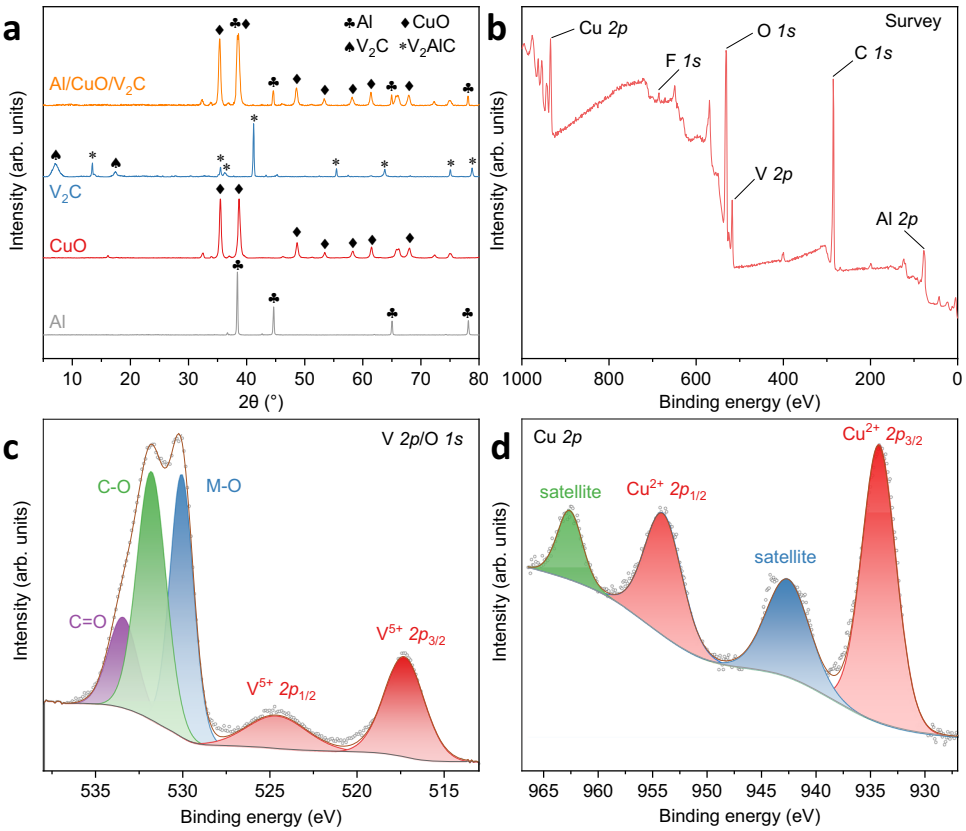

Fig. 2 | PXRD and XPS characterization of Al/CuO/V_2C. a Comparison of PXRD diffractograms of Al, CuO, V_2C, and Al/CuO/V_2C (10 wt% V_2C content). **b** XPS survey scan of Al/CuO/V_2C (10 wt%). **c** XPS fitted curves and deconvoluted peaks in V *2p*/O *1s* region for Al/CuO/V_2C (10 wt%). **d** XPS fitted curves and deconvoluted peaks in Cu *2p* region for Al/CuO/V_2C (10 wt%). Source data are provided as a Source Data file.

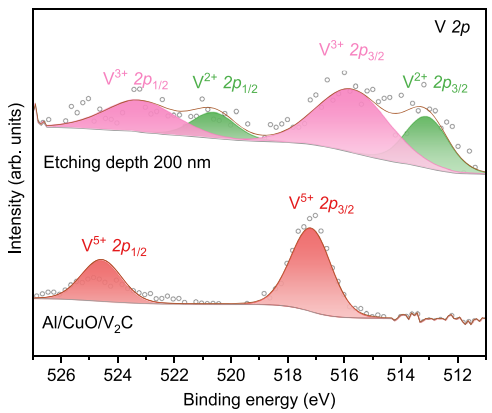

Fig. 3 | Composition of Al/CuO/V_2C after etching. XPS fitted curves and deconvoluted peaks in the V *2p* region for Al/CuO/V_2C (10 wt%) before (lower) and after (upper) etching at a depth of 200 nm. Source data are provided as a Source Data file.

gradually shifted the onset temperature of the first peak from 510 °C (1 wt%) to 560 °C (5 wt%), stabilizing at higher concentrations. Meanwhile, the onset temperature of the second peak remained unaffected by the addition of V_2C. The addition of V_2C significantly influences the thermite reaction dynamics in Al/CuO nanocomposites by delaying the onset of the first exothermic peak. This delay is attributed to the high thermal conductivity of V_2C, which effectively dissipates heat from neighboring Al and CuO particles, thereby slowing down the reaction initiation. As the content of V_2C increases, there is a noticeable shift in the thermite reaction mechanism. The peak temperatures rise from 580 °C to 620 °C, indicating a transition from a pure Al/CuO reaction to one involving vanadium compounds, specifically Al/CuO/V_2O_5. This change suggests that V_2C plays a role in altering the reaction pathway[29]. The second exothermic peak exhibits more complex behavior as V_2C concentration increases. It splits into two distinct peaks at 770 °C and 790 °C, corresponding to separate reactions: one between Al and CuO, and another between Al and V_2O_5. This observation aligns with literature findings that pure Al/CuO nanoparticles exhibit a peak around 760 °C under similar heating conditions[9]. Furthermore, the emergence of a new exothermic peak at ~ 790 °C as V_2C concentration increases is consistent with the reaction between liquid Al and V_2O_5[29,42]. This reaction's temperature varies between 797 °C and 840 °C, likely due to differences in particle size affecting reaction kinetics.

Based on the integration of DSC curves (Fig. 4b), the heat release increases with V_2C concentration from 1 wt% (1300 J g^{-1}) to 10 wt% (3156.2 J g^{-1}), then decreases at 20 wt% (1600 J g^{-1}). The addition of V_2C enhances the heat release by a factor of seven in the Al/CuO thermite reaction. Furthermore, the contribution of the second exothermic peak to the total heat release increases significantly with higher V_2C concentrations, rising from 45% at 1 wt% to 70% at 10 wt%. While the heat generated by the oxidation of aluminum (10870.4 J g^{-1}, Supplementary Fig. 5) and V_2C (6471.3 J g^{-1}, Supplementary Fig. 6) contributes to the total reaction heat, the observed heat release exceeds the sum of these individual contributions, suggesting a catalytic effect of V_2C in enhancing the reaction efficiency.

Based on the TG curves (Fig. 4c), the thermite reaction involving Al/CuO/V_2C in an air atmosphere can be divided into three distinct

https://doi.org/10.1038/s41467-025-60846-7

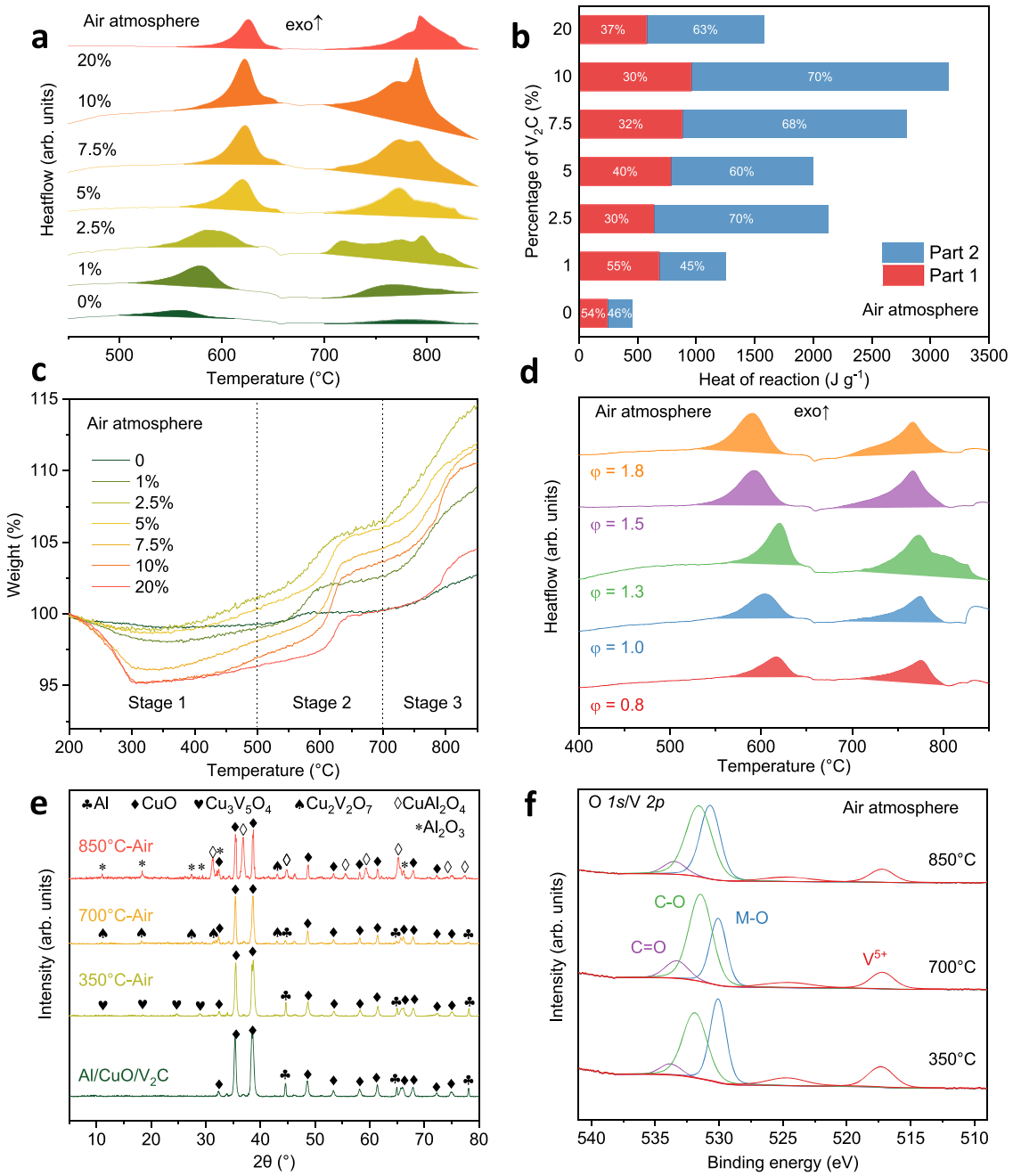

Fig. 4 | Thermal analysis on the temperature-dependent reaction process of Al/CuO/V_2C. a The DSC curves of Al/CuO/V_2C with the concentration of V_2C vary from 0 – 20 wt%, the exothermic peaks are upward. **b** The heat of reaction for Al/CuO/V_2C with the percentage of V_2C vary from 0 – 20 wt%. Parts 1 and 2 represent the first and second exothermic peaks shown in (**a**), respectively. **c** The DSC curves of Al/CuO/V_2C (10 wt% V_2C content) with equivalent ratio (Φ) from 0.8 to 1.8. **d** The TG curves correspond to the same samples in (**a**). **e** The PXRD curves of reaction products of Al/CuO/V_2C (10 wt% V_2C content) heating at different temperatures. **f** Deconvoluted XPS peaks at O *1s*/V *2p* region for reaction products of Al/CuO/V_2C (10 wt% V_2C content) heating at different temperatures, the original data and fitted curves are hidden for clarity. All measurements are performed in an air atmosphere. Source data are provided as a Source Data file.

stages. Between 200 °C and 500 °C (Stage 1), weight loss occurs primarily due to the loss of functional groups in V_2C, as previously reported in literature[25,43]. This weight loss during Stage 1 exhibits a linear relationship with the concentration of V_2C (Supplementary Fig. 7a). In Stage 2 (500–700 °C), the TG curves align with the onset temperatures of the exothermic peaks observed in DSC analysis. The maximum weight gain during this stage, attributed to the oxidation of Al and V_2C, is linearly correlated with the heat release, as demonstrated in Supplementary Fig. 7b. During the final stage (700 – 850 °C), the heat of reaction continues to increase alongside the weight gain of the samples, as illustrated in Supplementary Fig. 7c. This relationship shows that the rate of weight gain increases with higher concentrations of V_2C among the samples, as indicated by the dashed lines. As shown in Supplementary Fig. 7d, the slope of the 1 wt% V_2C sample is similar to that observed in Stage 2. However, the reaction heat per unit mass continues to increase up to a concentration of 20 wt%.

The samples with different equivalent ratios (Φ) exhibit distinct behaviors. For the Al/CuO/V_2C samples containing 5 wt% V_2C, the DSC curves (Fig. 4d) show that the heat release is maximized when aluminum is slightly in excess (Φ = 1.3). In contrast, a deficiency of fuel

(Φ = 0.8, 1.0) has a greater impact on the heat release of Al/CuO/V_2C compared to a deficiency of oxidant (Φ = 1.5, 1.8). In addition, the reaction heat in the first exothermic peak (part 1) increases with Φ, while the second peak (part 2) reaches its maximum at Φ = 1.3 (Supplementary Fig. 8). The involvement of external oxygen contributes to the first exothermic peak by oxidizing the aluminum nanoparticles between 500 °C and 700 °C. This is further illustrated in Supplementary Fig. 8, where the total heat release is compensated by part 1 as the proportion of Al increases. Consequently, the total heat release decreases more slowly in fuel-rich cases (Φ = 1.5, 1.8) than in oxygen-rich ones (Φ = 0.8, 1.0). During this stage, V_2C is also oxidized by air, providing additional heat release. Therefore, V_2C is considered to act as a fuel rather than an oxidant.

To better understand the role of V_2C in the reaction process, we analyzed the reaction products from samples containing 10 wt% V_2C after heating them to different temperatures in an air atmosphere, using PXRD for characterization (Fig. 4e). The results reveal that at 350 °C, following the release of surface terminations, a small amount of $Cu_3V_5O_4$ is detected due to the reaction between CuO and V_2C[44]. At 700 °C, the peak intensity of Al decreases sharply, while that of CuO remains, and a small amount of $Cu_2V_2O_7$ is detected[45]. This suggests the oxidation of Al and V_2C, as well as a reaction between CuO and V_2O_5. At 850 °C, Al_2O_3 appears as Al is fully oxidized, and $CuAl_2O_4$ is detected due to a reaction between CuO and Al_2O_3 at high temperatures[46,47]. The formation of copper vanadate is particularly noteworthy. Based on sample morphology, CuO exhibits a high affinity for the V_2C surface, providing opportunities for copper vanadate formation. Once formed at the interface, oxygen can readily diffuse from V_2O_5 to CuO through Cu-O-V bonds, shifting the mechanism from Al/CuO to Al/CuO/V_2O_5. XPS analysis of the reaction product (Fig. 4f) shows that the intensity of V^{5+} remains consistent during the reaction, compared to reactions in an argon atmosphere with varying V_2C concentrations (Supplementary Fig. 9). This indicates the high reactivity of the V_2C surface in absorbing oxygen from the air and preventing reduction during the reaction. Overall, exothermic reactions are significantly influenced by external oxygen. In the air atmosphere, during the first exothermic reaction from 500 °C to 700 °C (Stage 2), Supplementary Fig. 7b demonstrates that the heat of reaction is linearly correlated with the maximum weight gain in Stage 2, indicating that this exothermic reaction is primarily the oxidation of aluminum and V_2C by external oxygen:

$$4Al + 3O_2 \xrightarrow{500\sim700\,^{\circ}C} 2Al_2O_3 \quad (1)$$

$$CuO + 2V_2C + 7O_2 \xrightarrow{500\sim700\,^{\circ}C} 2Cu_2V_2O_7 + 2CO_2 \quad (2)$$

For the second exothermic reaction occurring between 700 and 850 °C (Stage 3), the heat of reaction increases with the weight gain of the samples, as shown in Supplementary Fig. 7c. This suggests that the oxidation of liquid-phase Al by air contributes to the reaction. However, this stage is more complex than the previous ones due to the involvement of ternary thermite reactions among Al, CuO, V_2O_5, and various valence states of vanadium oxide (VO_x)[42]. Notably, the increase in heat relative to weight gain becomes more pronounced as the concentration of V_2C in the samples rises (indicated by dashed lines). Supplementary Fig. 7d shows that the slope for the 1 wt% sample is similar to that of Stage 2, while the reaction heat per unit mass continues to increase up to 20 wt%. This indicates a reaction distinct from the simple oxidation of aluminum by air.

Based on the PXRD analysis of the reaction products (Fig. 4e), we propose the following reaction mechanism:

$$4Al + Cu_2V_2O_7 + 3O_2 \xrightarrow{700\sim850\,^{\circ}C} 2CuAl_2O_4 + V_2O_5 \quad (3)$$

This reaction accounts for the weight gain being less than that observed in Stage 2 and aligns with the experimental results. According to the XPS data (Fig. 4f), V_2O_5 is not reduced, as evidenced by the consistent intensity of the V^{5+} peak in the V *2p* region at both 700 °C and 850 °C.

The effect of the atmosphere on the thermite reaction involving Al/CuO/V_2C was analyzed using DSC and TG curves. In an argon atmosphere, two types of thermite reactions were observed between 300 °C and 800 °C, as indicated by a dashed line (Supplementary Fig. 10). For concentrations below 5 wt%, the behavior mirrored that in air, while higher concentrations exhibited subtler reactions with distinct exothermic peaks. The onset temperature advanced to 400 °C for the 10 wt% sample. TG curves in argon (Supplementary Fig. 11) revealed the detachment of V_2C surface terminations before 350 °C (Stage 1). Without environmental oxygen, exothermal reactions were primarily due to the thermite reaction between Al and CuO. Comparing air and argon atmospheres using Supplementary Fig. 12a and Supplementary Fig. 12b shows the differences in the first exothermic peaks. In argon, the absence of a step-like weight gain between 500–600 °C indicated a solid-solid reaction, as per literature[9]. The second peak beyond the melting point (Stage 3) represented the Al/CuO liquid-solid thermite reaction from 660–800 °C. Weight loss in Stage 1 was due to V_2C termination detachment. Slower weight gain in Stage 2 resulted from reduced oxidation by outside oxygen, though V_2C could still oxidize via terminations or interlayered water in inert atmospheres[43,48]. For 10 wt% samples, four exothermal peaks were observed between 400–700 °C in argon. PXRD results (Supplementary Fig. 13) attributed the first peak (400–500 °C) to the Al/CuO solid phase thermite reaction, reducing CuO to Cu_2O. The advanced onset temperature was due to alumina shell etching by fluoride-containing termination groups[11]. The second and third peaks resulted from Al reacting with Cu_2O to reduce it further to Cu. VO_x oxidized from V_2C may also react with Al to generate low-valence V. The fourth peak at 650 °C, marked by a steep rise, was due to the increased reaction rate of the Al/Cu_2O thermite reaction as aluminum melted. Different stages of reactions are detailed in Supplementary Fig. 12d. Unlike air atmosphere samples showing step-like features due to environmental oxygen involvement, argon samples exhibited no obvious weight change during reactions.

In argon atmosphere, the exothermic reactions for 10 wt% samples can be summarized as follows:

$$2Al + 6CuO \xrightarrow{400\sim500\,^{\circ}C} Al_2O_3 + 3Cu_2O \quad (4)$$

$$2Al + 3Cu_2O \xrightarrow{500\sim700\,^{\circ}C} Al_2O_3 + 6Cu \quad (5)$$

Outside, oxygen first oxidizes Al, which corresponds to the first exothermic peak. Subsequently, outside oxygen fully oxidizes V_2C into V_2O_5, leading to the formation of $Cu_2V_2O_7$, which then reacts with Al, represented by the second exothermic peak. This explains why higher concentrations of V_2C hinder heat release in argon: excess V_2C cannot be fully oxidized and does not aid in oxidizing Al, thereby reducing the proportion of Al and CuO available for reaction.

Energetic Performance of Al/CuO/V_2C

An open burn experiment was conducted to evaluate the energetic performance of Al/CuO/V_2C composites (Supplementary Movie 1–4). The Al/CuO sample without V_2C addition burned for a total duration of 6 ms, with the flame reaching its maximum intensity at 1 ms (Fig. 5a). Upon adding 1 wt% V_2C, the total burning time was halved to 3 ms, and the flame reached its peak intensity at 0.4 ms, accompanied by a significant increase in the covered area (Fig. 5b). For the sample

https://doi.org/10.1038/s41467-025-60846-7

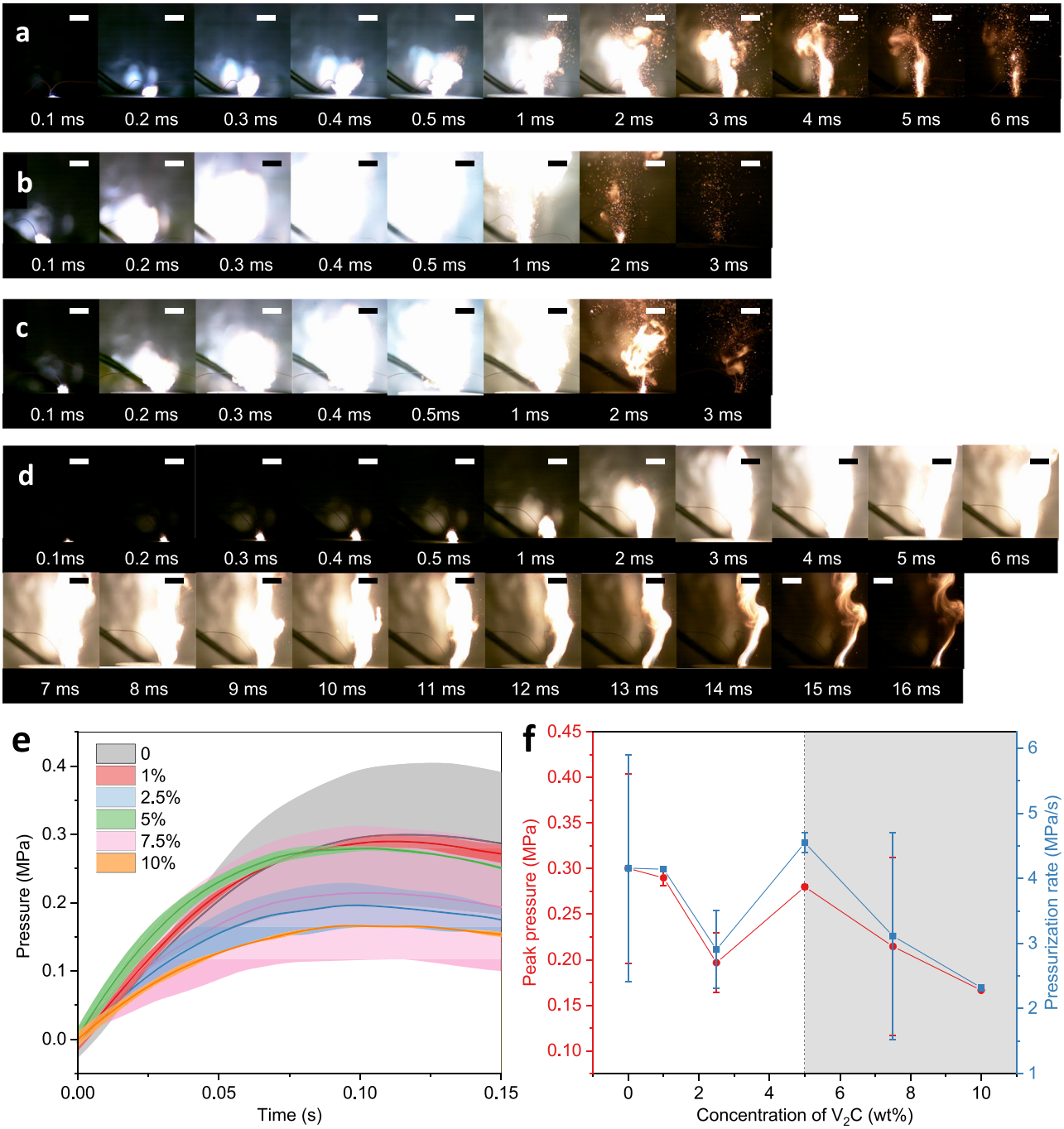

Fig. 5 | Energetic performance of Al/CuO/V_2C. a–d The open burn results of Al/CuO (**a**), Al/CuO/V_2C with 1 wt% V_2C content (**b**), Al/CuO/V_2C with 5 wt% V_2C content (**c**), Al/CuO/V_2C with 10 wt% V_2C content (**d**). Scale bar: 10 mm. **e** Dynamic pressure for Al/CuO/V_2C samples with different concentrations of V_2C, each error band consists of two tests. **f** The peak pressure and pressurization rate of Al/CuO/V_2C samples from two tests, the gray region in (**f**) is to highlight the difference between low and high concentrations. The mean values and standard deviations in (**e**) (**f**) are derived from two biological replicates, data are presented as mean values +/− SD as appropriate. The data used to calculate the center of the error band and SD in (**e**) is obtained from the pressures of two tests at the same time. The experiments for (**a**–**d**) were repeated three times independently with similar results. Source data are provided as a Source Data file.

containing 5 wt% V_2C, the burning performance was comparable to that of the 1 wt% sample, with only a slight delay in ignition. The maximum coverage occurred at 0.5 ms (Fig. 5c). As the concentration of V_2C increased further, the flame characteristics changed significantly. In the case of the 10 wt% V_2C sample, instead of an explosive reaction as observed in lower concentration samples, the material burned steadily until the reaction was complete, resulting in a flame that lasted for 16 ms (Fig. 5d). At low concentrations of V_2C, the Al/CuO/V_2C composite forms a planar structure where Al and CuO nanoparticles are sequentially attached to the V_2C surface. This arrangement reduces nanoparticle agglomeration, increasing the contact area between Al and CuO particles. Consequently, the average oxygen diffusion rate is enhanced, leading to shorter burning times and higher energy release rates. However, at high concentrations of V_2C, the composite adopts a quasi-spherical structure with V_2C forming a shell encapsulating Al and CuO nanoparticles both inside and

outside. This structural change restricts the free explosion of internal particles, significantly reducing the reaction rate from explosive to combustion mode. Despite this reduction in reactivity, it results in a substantial increase in energy release efficiency and duration.

The energetic performance of Al/CuO/V_2C can be significantly adjusted by varying the concentration of V_2C during fabrication. Introducing a low concentration of V_2C (from 1 to 5 wt%) enhances the reaction rate and reduces the overall reaction time by approximately half. Conversely, increasing the concentration to 10 wt% slows down the reaction rate and extends the reaction duration to nearly three times its original length. In addition, the burning behavior can be modulated from a more intense explosion at lower concentrations to a calmer combustion process at higher concentrations. This versatility makes Al/CuO/V_2C nanothermite suitable for both primary explosive and microinitiator applications.

Lowering the pressure is essential for nanothermite in both safety and microinitiator applications[1]. Therefore, a closed-bomb test was conducted to evaluate the combustion properties in a confined space and assess the gas-generating ability of Al/CuO/V_2C samples. The dynamic pressure of Al/CuO/V_2C samples is lower than that of Al/CuO, with a peak at 0.1 s (Fig. 5e). This reduced pressure is primarily due to the introduction of gasless V_2C and partly because of insufficient oxygen, which slightly alters the reaction mechanism. The test results with calculated mean values and standard deviations for each concentration are provided (Supplementary Fig. 14). The pressurization rate follows the same trend as the peak pressure for Al/CuO/V_2C samples (Fig. 5f). Generally, both the peak pressure and pressurization rate decrease as the concentration of V_2C increases. However, these parameters also depend on the structure of Al/CuO/V_2C (gray region). The overall trend is mainly caused by a reduction in gas generation since the decomposition of V_2C contributes little to gaseous products. Interestingly, the peak pressure and pressurization rate of Al/CuO/V_2C with 5 and 7.5 wt% concentrations are similar to those of the 1 wt% sample, highlighting the role of structural differences. The peak pressure and pressurization rate of Al/CuO/V_2C were reduced by 44.5% and 44.1%, respectively (comparing the mean values of 0 and 10 wt% samples). This significant reduction indicates that V_2C can greatly enhance the safety of Al/CuO and is feasible for microinitiator applications.

Binding mechanism analysis of Al/CuO/V_2C

The tunable performance of Al/CuO/V_2C nanothermites is attributed to their unique structures arising from ordered self-assembly. To investigate this mechanism, various samples (Al/V_2C and CuO/V_2C, Supplementary Fig. 15) were characterized using PXRD, Raman spectroscopy, Fourier transform – infrared spectroscopy (FT-IR), and XPS. Raman spectroscopy revealed a characteristic peak at 895 cm^{-1}, indicative of Cu-O-V bonds at the CuO/V_2C interface (Fig. 6a)[27]. The absence in the Al/CuO/V_2C spectrum is probably because the CuO/V_2C interface is more densely covered. In addition, FT-IR analysis detected -CH_2-CH_2- vibrations[49], suggesting residual carbon nanosheets after V-C bond cleavage, supporting the presence of covalent interactions (Fig. 6b). XPS analysis (Fig. 6c) further confirmed these findings with shifts in Cu^{2+} $2p_{3/2}$ and Cu^{2+} $2p_{1/2}$ orbits to higher binding energies, consistent with Cu-O-V bond formation[50]. In contrast, Al nanoparticles exhibited weaker binding strength and a more randomized distribution around CuO/V_2C, suggesting an electrostatic assembly mechanism. Zeta potential analysis (Fig. 6d) corroborated this by showing positive potentials for Al and CuO particles and negative for V_2C suspension. At low V_2C concentrations (1 – 5 wt%), the system's zeta potential remained positive, indicating minimal influence on overall charge but reduced nanoparticle agglomeration. However, at higher concentrations (10 – 20 wt%), the zeta potential dropped sharply, suggesting charge neutralization by V_2C. These findings align with experimental results (Fig. 1), highlighting that covalent Cu-O-V interactions are shorter and stronger than electrostatic attractions between Al and V_2C. This comprehensive characterization underscores the interplay of covalent and electrostatic mechanisms in the assembly process of Al/CuO/V_2C nanothermites.

The thermite reaction involving Al/CuO/V_2C nanothermite is significantly influenced by their binding properties and layered structure. This structure enhances oxygen diffusion, a critical factor in facilitating the reaction. In contrast (Fig. 6e), an Al/CuO nanocomposite exhibits incomplete reactions due to random particle assembly and agglomeration, which reduce the contact area between aluminum and copper oxide. In the case of Al/CuO/V_2C (Fig. 6f), the layered architecture allows for efficient oxygen migration from CuO to aluminum particles. In addition, in an air atmosphere, oxygen is replenished through Cu-O-V bonds with V_2C, ensuring complete oxidation of Al into Al_2O_3. This conclusion is supported by PXRD analysis comparing Al/CuO/V_2C with a control group, revealing residual aluminum peaks at 850 °C in the latter (Supplementary Fig. 16). To further illustrate the benefits of ordered self-assembly over traditional methods, a control group using V/GO instead of V_2C was tested. The DSC curves for this group showed distinct exothermic peaks for Al/V_2O_5 (622 °C) and Al/CuO (567 °C), indicating poor component interactions and incomplete reactions, resulting in lower heat release (Supplementary Fig. 17). In summary, V_2C not only enhances the structure but also improves the reactivity of Al/CuO nanothermite. Its structural evolution opens new possibilities for future applications, offering a more efficient and effective thermite reaction compared to previously used additives.

Discussion

In conclusion, Al/CuO/V_2C nanocomposite has been successfully prepared with unique structures resulting from the ordered self-assembly of Al and CuO nanoparticles. This structure evolves from planar to quasi-spherical as the concentration of V_2C increases from 1% to 10% (wt%). During the self-assembly process, CuO exhibits a higher affinity to the V_2C surface compared to Al, leading to a layered structure. The synergistic effect of the two-dimensional (2D) structure and the high reactivity of V_2C results in a delayed onset temperature for the exothermic reaction by 60 °C. Heat release increases sevenfold, reaching 3156.2 J g^{-1} for Al/CuO/V_2C compared to 454.4 J g^{-1} for Al/CuO in an air atmosphere. The reaction mechanism shifts from Al/CuO to Al/CuO/V_2O_5. The burning behavior of Al/CuO/V_2C changes significantly with varying concentrations of V_2C, transitioning from an explosive reaction lasting 3 ms to a sustained combustion lasting 16 ms. This results in a 44.5% reduction in peak pressure compared to Al/CuO. The ordered self-assembly of Al/CuO/V_2C arises from differing bonding interactions: electrostatic forces between Al and V_2C, and covalent bonds between CuO and V_2C. This structural arrangement enhances oxygen transport efficiency and ensures complete oxidation of aluminum.

Methods

Materials

The nano aluminum powder is purchased from Zhonghangzhongmai Metal Material Inc. with a diameter range from 80 – 200 nm (Supplementary Fig. 18), and an active content of 80%. The nano copper oxide powder is self-made using the thermal pyrolysis method at 300 °C for 90 min from $Cu(OH)_2$, with a diameter range from 80 – 100 nm (Supplementary Fig. 19). The V_2C MXene single-layer suspension is purchased from Shandong Xiyan Material Inc. with a concentration of 10 mg mL^{-1}, dispersed in DMF (Supplementary Fig. 20). The XPS data of V_2C is provided (Supplementary Fig. 21). The absolute alcohol is purchased from Standard Chemical Inc. (ACS grade). Vanadium powder is purchased from Aladdin Inc., 99.5% metals basis, ≥ 325 mesh. Graphene oxide powder is purchased from Aladdin Inc., > 99%. All chemicals are used without further purification.

https://doi.org/10.1038/s41467-025-60846-7

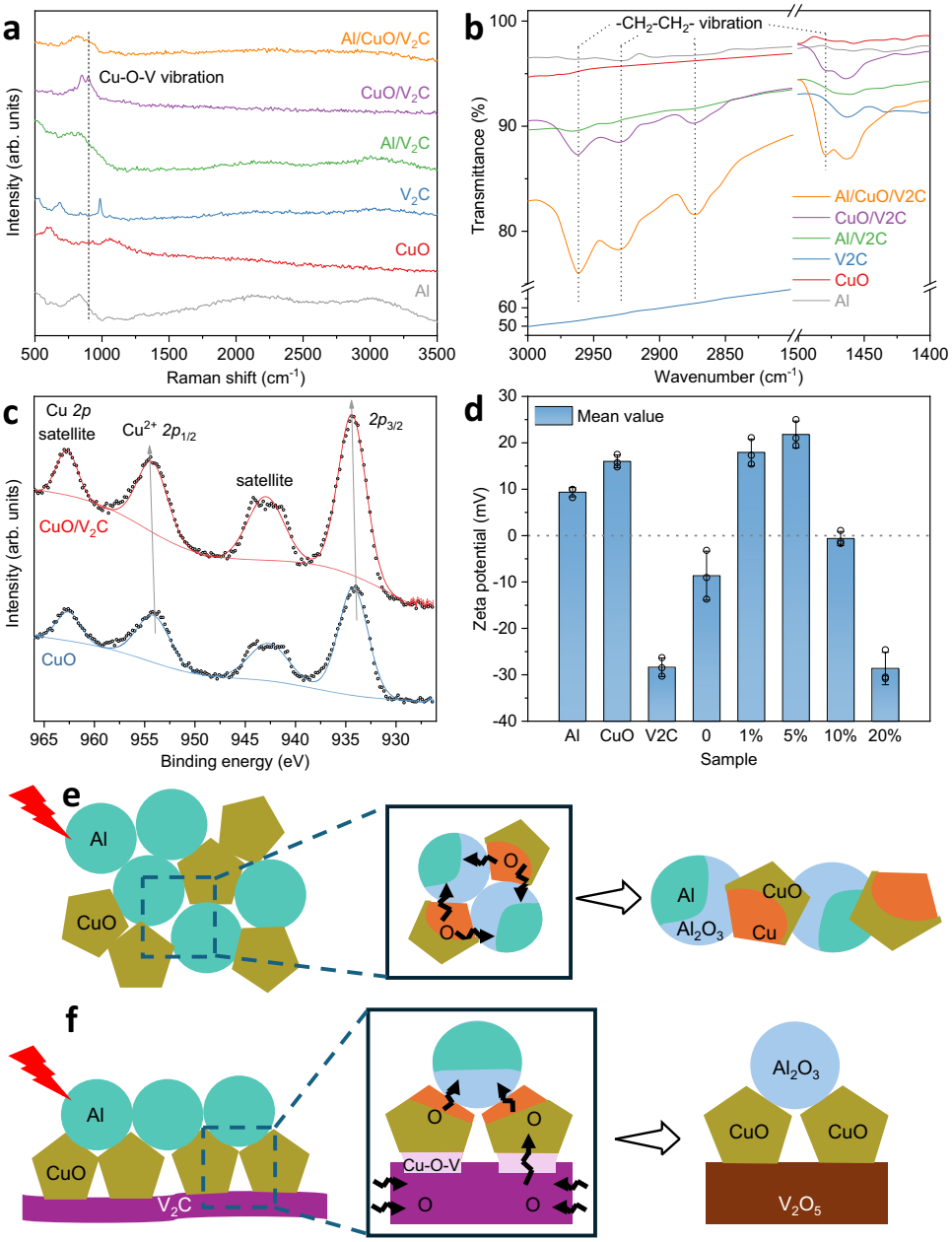

Fig. 6 | Binding mechanism of Al/CuO/V_2C. a The Raman spectra of Al, CuO, V_2C, Al/V_2C, CuO/V_2C, and Al/CuO/V_2C (10 wt% V_2C content), the dashed line represents the Cu-O-V vibrational peak. **b** The FT-IR spectra of Al, CuO, V_2C, Al/V_2C, CuO/V_2C, and Al/CuO/V_2C, the dashed lines represent -CH_2-CH_2- vibrational peaks. **c** Comparison of CuO/V_2C and Al/CuO/V_2C XPS curves in Cu *2p* region, the gray arrows represent the direction of the shift of Cu^{2+} *2p* peaks. **d** The mean values of zeta potential of different samples: Al, CuO, V_2C, Al/CuO, Al/CuO/V_2C with concentration of V_2C from 1–20%. **e** Illustration of the oxygen diffusion pathway during the thermite reaction of the Al/CuO sample. **f** Illustration of the oxygen diffusion pathway during the thermite reaction of the Al/CuO/V_2C sample. The mean values and standard deviations in (**d**) are derived from three biological replicates, data are presented as mean values +/− SD as appropriate. Source data are provided as a Source Data file.

Preparation of V_2C MXene

The etching method used by the supplier Shandong Xiyan Material Inc. to produce the purchased V_2C from V_2AlC is as follows: 1 g material is added with 10 ml of 50% hydrofluoric acid solution and stirred at 35 °C for 48 h. Deionized water is added to the solution, centrifuging 5-7 times. Then the wet V_2C is dissolved in 10 ml of isopropyl amine (IPA) and stir at room temperature for 24 h. Next, the material is centrifuge once (note that it is once), adding 100 ml of DMF (or 50) and ultrasonicate for 1-2 h. Finally, the solution is centrifuged at 1301 × *g* for 1 h to obtain a colloidal product. The precipitate can be ultrasonicated repeatedly or discarded.

V_2C samples are further prepared from the purchased V_2C suspension by our group. For centrifuged V_2C samples, firstly, 5 mL of the 10 mg mL^{-1} V_2C suspension is transferred to a centrifuge tube. Then, 20 mL absolute alcohol is added into the centrifuge tube, and the tube is centrifuged at 956 × *g* for 3 min. Next, the liquid supernatant is removed, and another 20 mL absolute alcohol is added. Then, the tube is centrifuged at the same speed and time. Finally, the supernatant is removed, and the precipitate is dried in the vacuum oven at 60 °C overnight. For freeze-dried samples, 3 mL of the 10 mg mL^{-1} V_2C suspension is transferred to a sample dish. Then, the sample is freeze-dried for 24 h. For liquid samples, approximately 1 mL of the

10 mg mL^{-1} V_2C suspension is directly added on the testing glass slide to fill the groove. Then the slide is attached to the XRD equipment, and the test is performed.

Preparation of Al/CuO/V_2C

The composition of all samples is listed in Supplementary Table S1. For the typical preparation procedures of Al/CuO/V_2C with 10 wt% V_2C, in the Φ = 1.3 case, firstly, 20.4 mg Al powder is added into 5 mL absolute ethanol as suspension A, 69.6 mg CuO powder is added into 5 mL absolute ethanol as suspension B, 1 mL V_2C suspension is added into 10 mL absolute ethanol as suspension C. Then, A, B, and C are sonicated for 1 h. Next, both A and B are added into C, and C is sonicated for another 1 h. After that, C is placed in the vacuum oven and dried overnight at 60 °C. Finally, C is collected as the sample.

Preparation of Al/CuO/V/GO

In the Φ = 1.3, 10 wt% V/GO case, suspension C is comprised of a mixture of 9 mg V powder and 1 mg GO powder dispersed in 10 mL absolute ethanol. Other materials and procedures are identical to those of Al/CuO/V_2C.

Preparation of Al/V_2C and CuO/V_2C

For a better comparison, Al/V_2C and CuO/V_2C samples are prepared using the same materials and methods for Al/CuO/V_2C without the addition of CuO or Al. For example, 20.4 mg Al powder and 10 mg V_2C are mixed for Al/V_2C, 69.6 mg CuO and 10 mg V_2C are mixed for CuO/V_2C as the control group of Al/CuO/V_2C with 10 wt% content and Φ = 1.3.

Characterization of Al/CuO/V_2C

Scanning electron microscopy (SEM) pictures are taken with a Quanta FEI 450. Transmission electron microscopy (TEM) and high-resolution scanning transmission electron microscopy high-angle annular dark-field (STEM-HAADF) images are gathered by FEI Talos F200x, samples are dispersed in ethanol and sonicate for 1 min before testing. The interplanar spaces of high-resolution TEM images are obtained by DigitalMicrograph. X-ray photoelectron spectroscopy (XPS) is performed with Thermo Scientific K-Alpha. The data are analyzed by CasaXPS and Origin. Powder X-ray diffraction (PXRD) is performed with Rigaku SmartLab from 5 − 80° at 30 kV using Cu Kα radiation (λ = 0.15418 nm). The data are analyzed by Jade and Origin. The thermogravimetry (TG) and differential scanning calorimetry (DSC) results are acquired by METTLER TGA/DSC 3 +, which records the weight and heat flow of one sample simultaneously. For each test, around 2 mg samples are put into a 50 μL alumina crucible and then heated at a heating rate of 10 °C min^{-1} under high-purity air or argon flow (20 mL min^{-1}). To obtain comparable data, all DSC curves are divided by the sample weight at 60 °C. The data are analyzed by Origin. Raman analysis was done with a confocal Raman microscope (CRM) (Alpha300R, WITec GmbH, Germany) equipped with a TEM single-frequency laser (λ = 532 nm, laser power = 40 mW, WITec GmbH, Germany). The laser light was focused through a 100x oil immersion objective (numerical aperture = 0.9) (Carl Zeiss, Germany) onto the sample and the backscattered Raman signal directed through an optic multifibre (50 μm diameter) to a spectrometer (UHTS 300 WITec, Germany) (300 g mm^{-1} grating) and detected by the CCD camera (Andor DU401 BV, Belfast, North Ireland). On the selected areas (e.g., 30 μm x 20 μm) on the sample every 0.5 μm a full wavenumber range (50 − 4000 cm^{-1}) Raman spectrum was acquired with an integration time of 1 s. The Control Five (WITec GmbH, Germany) acquisition software was used for the Raman measurements set up, and Project Five (WITec GmbH, Germany) to reconstruct Raman images based on the integral band of the ester group at 1734 cm^{-1} and the hydroxyl groups at 3400 cm^{-1}. The data are analyzed by Origin. Fourier-transform infrared spectroscopy (FT-IR) is conducted with Thermo Fisher Scientific Nicolet iS5 in the range of 400 − 4000 cm^{-1}, in which all samples are dried at 65 °C for 1 h to remove water before testing. The data are analyzed by OMNIC and Origin. Zeta potentials are acquired by the Malvern Zetasizer Nano ZS90. Samples are dispersed in ethanol to form a 1 − 2 mg mL^{-1} suspension and sonicate for 30 min before testing, and 1 mL suspension is used for each test. The data are analyzed by Origin.

Open burn test of Al/CuO/V_2C

All samples are grounded and dried at 60 °C before testing. A PTFE cylinder mold is made with a height of 10 mm and a diameter of 50 mm, and a cylinder hole at the center with a height of 5 mm and a diameter of 6 mm (Supplementary Fig. 22). For each test, an alumina crucible with a height of 5 mm and diameter of 5 mm is filled with 6 mg of the sample and then placed in the hole of the PTFE mold. The charging density is 0.5 g cm^{-3}. The environment pressure is 1 bar, in air atmosphere. Next, a nichrome wire with a diameter of 0.2 mm is connected to the power source set with a current of 2.7 A and is buried in the crucible to make full contact with the sample. The shutter of the high-speed camera and the power source are pressed simultaneously to capture the flame. Once the power source is opened, the sample is ignited, and the process is captured by the high-speed camera (Phantom, VEO 710) with 10000 FPS and an exposure time of 20 μs. To measure the burning time, the frame before the flare is chosen as the beginning of burning, and the frame before the flame detaches from the crucible is selected as the end of burning. The data are collected and analyzed by PCC and Origin.

Closed-bomb test of Al/CuO/V_2C

All samples are grounded and dried at 60 °C before testing. Typically, a 20 mg sample is gathered in the confined cell made of stainless steel with a fixed volume of 8 mL and subsequently ignited by a nichrome wire (0.2 mm in diameter) under a 2.8 A current. The dynamic pressure during the reaction process is measured by a piezoelectric pressure sensor (PCB Piezotronics, Model 112B05) attached to the cell, and the pressure signal is transformed into a voltage signal through a signal conditioner (PCB Piezotronics, Model 482C54), and then recorded by the oscilloscope (Tek, DPO3032). The sample is gathered at the center of the chamber with a square shape and a 1 cm length of side. The height of the sample is approximately 0.2 cm. The charging density of the sample is 0.1 g cm^{-3}. The data are analyzed by Origin.

Reporting summary

Further information on research design is available in the Nature Portfolio Reporting Summary linked to this article.

Data availability

All data generated in this study are provided in the Source Data File. Source data are provided in this paper.

References

1. He, W., Liu, P. J., He, G. Q., Gozin, M. & Yan, Q. L. Highly reactive metastable intermixed composites (MICs): Preparation and characterization. *Adv. Mater.* **30**, e1706293 (2018).
2. Ma, X. et al. Core-shell structured nanoenergetic materials: Preparation and fundamental properties. *Adv. Mater.* **32**, e2001291 (2020).
3. Wang, A., MacRobbie, C. J., Baranovsky, A., Hickey, J.-P. & Wen, J. Z. Microstructure and energetic characteristics of direct ink printed polymer-free rGO/nanothermite aerogel. *Carbon* **216**, 118596 (2024).
4. Wang, H. et al. Direct writing of a 90 wt% particle loading nanothermite. *Adv. Mater.* **31**, e1806575 (2019).
5. Shi, K. et al. Alcohol-thermal synthesis of approximately core-shell structured Al@CuO nanothermite with improved heat-release and combustion characteristics. *Combust. Flame* **228**, 331–339 (2021).

6. Shi, W. et al. Enhancing the energy release performance of nano-thermites through metal oxides free oxygen and pores. *Chem. Eng. J.* **481**, 148483 (2024).
7. Ma X., et al. Additive-free energetic film based on graphene oxide and nanoscale energetic coordination polymer for transient microchip. *Adv. Funct. Mater.* **31**, https://doi.org/10.1002/adfm.202103199 (2021).
8. Jiang, Y. et al. Perfluoroalkyl-functionalized graphene oxide as a multifunctional additive for promoting the energetic performance of aluminum. *ACS Nano* **16**, 14658–14665 (2022).
9. Chen, Y. et al. Reactivity adjustment from the contact extent between CuO and Al phases in nanothermites. *Chem. Eng. J.* **402**, 126288 (2020).
10. Singh, V. et al. Influence of process parameters on energetic properties of sputter-deposited Al/CuO reactive multilayers. *Nanotechnology* **33**, 465704 (2022).
11. Li, Y. et al. Synthesis of Co(OH)F@Al nanobelt array on various substrates for pyro-MEMS. *Chem. Eng. J.* **466**, 143192 (2023).
12. Zhu, Y. et al. In situ preparation of explosive embedded CuO/Al/CL20 nanoenergetic composite with enhanced reactivity. *Chem. Eng. J.* **354**, 885–895 (2018).
13. Wang, W. et al. Effects of oxidizer and architecture on the thermochemical reactivity, laser ignition and combustion properties of nanothermite. *Fuel* **314**, 123141 (2022).
14. Fahd, A., Baranovsky, A., Dubois, C., Chaouki, J. & Wen, J. Z. Superior performance of quaternary NC/GO/Al/KClO4 nanothermite for high speed impulse small-scale propulsion applications. *Combust. Flame* **232**, 111527 (2021).
15. Kwon, J. et al. Interfacial chemistry in Al/CuO reactive nanomaterial and its role in exothermic reaction. *ACS Appl. Mater. Interfaces* **5**, 605–613 (2013).
16. Séverac, F., Alphonse, P., Estève, A., Bancaud, A. & Rossi, C. High-energy Al/CuO nanocomposites obtained by DNA-directed assembly. *Adv. Funct. Mater.* **22**, 323–329 (2011).
17. Tang, D.-Y. et al. Metastable intermixed Core-shell Al@M(IO3)x nanocomposites with improved combustion efficiency by using tannic acid as a functional interfacial layer. *Chem. Eng. J.* **384**, 123369 (2020).
18. Wei, Y., Zhang, P., Soomro, R. A., Zhu, Q. & Xu, B. Advances in the synthesis of 2D MXenes. *Adv. Mater.* **33**, e2103148 (2021).
19. Li, X. et al. MXene chemistry, electrochemistry and energy storage applications. *Nat. Rev. Chem.* **6**, 389–404 (2022).
20. Zhao, Y. et al. Engineering strategies and active site identification of MXene-based catalysts for electrochemical conversion reactions. *Chem. Soc. Rev.* **52**, 3215–3264 (2023).
21. Iqbal, A. et al. Anomalous absorption of electromagnetic waves by 2D transition metal carbonitride Ti3CNTx (MXene). *Science* **369**, 446–450 (2020).
22. VahidMohammadi, A., Rosen, J. & Gogotsi, Y. The world of two-dimensional carbides and nitrides (MXenes). *Science* **372**, https://doi.org/10.1126/science.abf1581 (2021).
23. Cheng, J. et al. Doping of Al/CuO with microwave absorbing Ti3C2 MXene for improved ignition and combustion performance. *Chem. Eng. J.* **451**, 138375 (2023).
24. Li, Y. et al. Adhesion Between MXenes and Other 2D Materials. *ACS Appl. Mater. Interfaces* **13**, 4682–4691 (2021).
25. Cao, F. et al. Recent advances in oxidation stable chemistry of 2D MXenes. *Adv. Mater.* **34**, e2107554 (2022).
26. Hou, P. et al. Unraveling the oxidation behaviors of MXenes in aqueous systems by active-learning-potential molecular-dynamics simulation. *Angew. Chem. Int. Ed. Engl.* **62**, e202304205 (2023).
27. Tian, H. et al. Selective electrooxidation of methane to formic acid by atomically dispersed CuOx and its induced Lewis acid sites on V_2O_5 in a tubular electrode. *Appl. Catal. B Environ. Energy* **351**, 124001 (2024).
28. Liu, B., Yu, L., Yu, F. & Ma, J. In-situ formation of uniform V_2O_5 nanocuboid from V_2C MXene as electrodes for capacitive deionization with higher structural stability and ion diffusion ability. *Desalination* **500**, 114897 (2021).
29. Streletskii, A. N. et al. Mechanochemical activation of Al/V_2O_5 composites: Thermal transformations. *Mater. Chem. Phys.* **292**, 126798 (2022).
30. Yang, B., Tang, P., Li, R., Li, X. & Yang, G. Reaction-dominated combustion control of ammonium perchlorate-based composites by layered V_2C MXene. *Energ. Mater. Front.* **3**, 199–208 (2022).
31. Huang, D. et al. Demonstration of a white laser with V(2) C MXene-based quantum dots. *Adv. Mater.* **31**, e1901117 (2019).
32. Liu, Y. T. et al. Self-assembly of transition metal oxide nanostructures on MXene nanosheets for fast and stable Lithium storage. *Adv. Mater.* **30**, e1707334 (2018).
33. Yang, J. et al. Electrostatic self-assembly of heterostructured black phosphorus–MXene nanocomposites for flexible micro-supercapacitors with high rate performance. *Energy Storage Mater.* **36**, 257–264 (2021).
34. Wang, X. et al. 2D/2D 1T-MoS2/Ti3C2 MXene Heterostructure with excellent supercapacitor performance. *Adv. Funct. Mater***30**, https://doi.org/10.1002/adfm.201910302 (2020).
35. Guo, D. et al. Covalent assembly of two-dimensional COF-on-MXene heterostructures enables fast charging Lithium hosts. *Adv. Funct. Mater.***31**, https://doi.org/10.1002/adfm.202101194 (2021).
36. Shan, Q. et al. Two-dimensional vanadium carbide (V_2C) MXene as electrode for supercapacitors with aqueous electrolytes. *Electrochem. Commun.* **96**, 103–107 (2018).
37. Li, X. et al. In situ electrochemical synthesis of MXenes without acid/alkali usage in/for an aqueous Zinc Ion battery. *Adv. Energy Mater.* **10**, https://doi.org/10.1002/aenm.202001791 (2020).
38. Zhou, J., Dahlqvist, M., Björk, J. & Rosen, J. Atomic scale design of MXenes and their parent materials horizontal line from theoretical and experimental perspectives. *Chem. Rev.* **123**, 13291–13322 (2023).
39. Mohapatra, D. et al. Process controlled ruthenium on 2D engineered V-MXene via atomic layer deposition for human healthcare monitoring. *Adv. Sci.***10**, e2206355 (2023).
40. Zada, S. et al. Algae extraction controllable delamination of vanadium carbide nanosheets with enhanced near-infrared photothermal performance. *Angew. Chem. Int. Ed. Engl.* **59**, 6601–6606 (2020).
41. Zhang, W. et al. Architecting amorphous vanadium oxide/MXene nanohybrid via tunable anodic oxidation for high-performance sodium-ion batteries. *Adv. Energy Mater.* **11**, https://doi.org/10.1002/aenm.202100757 (2021).
42. Shevchenko, V. G. et al. Effect of V_2O_5 on the oxidation mechanism of ASD-4 powder. *Combust. Explos. Shock Waves* **51**, 572–577 (2015).
43. Wu, M., Wang, B., Hu, Q., Wang, L. & Zhou, A. The synthesis process and thermal stability of V(2)C MXene. *Materials* **11**, 2112 (2018).
44. Shaheen, W. M. & Maksod, I. H. A. E. Thermal characterization of individual and mixed basic copper carbonate and ammonium metavanadate systems. *J. Alloy. Compd.* **476**, 366–372 (2009).
45. Guo, W. et al. Synthesis and characterization of CuV2O6 and Cu2V2O7: Two photoanode candidates for photoelectrochemical water oxidation. *J. Phys. Chem. C.* **119**, 27220–27227 (2015).
46. Zhang, T., Yuan, B., Wang, W., He, J. & Xiang, X. Tailoring *H intermediate coverage on the CuAl(2) O(4) /CuO catalyst for enhanced electrocatalytic CO(2) reduction to ethanol. *Angew. Chem. Int. Ed. Engl.* **62**, e202302096 (2023).
47. Jacob, K. T. & Alcock, C. B. Thermodynamics of CuAlO2 and CuAl2O4 and Phase Equilibria in the System Cu2O-CuO-Al2O3. *J. Am. Ceram. Soc.* **58**, 192–195 (2006).
48. Thakur, R. et al. Insights into the thermal and chemical stability of multilayered V(2)CT(x) MXene. *Nanoscale* **11**, 10716–10726 (2019).

49. Ţucureanu, V., Matei, A. & Avram, A. M. FTIR Spectroscopy for carbon family study. *Crit. Rev. Anal. Chem.* **46**, 502–520 (2016).
50. Gopalakrishnan, R., Chowdari, B. V. R., Tan, K. L. & Radhakrishnan, K. Surface and electrical studies of CuO: V_2O_5 thin films. *Thin Solid films* **260**, 161–167 (1995).

Acknowledgements

M.T., K.M., K.X., I.H., X.M., and K.Z. were supported by the Hong Kong Research Grants Council (CityU 11201522) and the Innovation and Technology Commission of HKSAR through the Hong Kong Branch of National Precious Metals Material Engineering Research Center.

Author contributions

M.T. and K.Z. devised and developed the research. M.T., K.M., and K.X. conducted the experiments. M.T., K.M., K.X., I.H., and X.M. performed material characterizations and analyzed the data. M.T. and K.M. wrote the manuscript. All authors contributed to general discussions and edited and reviewed the manuscript.

Competing interests

The authors declare no competing interests.

Additional information

Supplementary information The online version contains supplementary material available at https://doi.org/10.1038/s41467-025-60846-7.

Correspondence and requests for materials should be addressed to Kaili Zhang.

Peer review information *Nature Communications* thanks Ruiqi Shen and the other anonymous reviewer(s) for their contribution to the peer review of this work. A peer review file is available.